Applied Surface Science 356 (2015) 128–134

Contents lists available at ScienceDirect

Applied Surface Science

journal homepage: www.elsevier.com/locate/apsusc

Interaction between phosphate and acid-activated neutralized red mud during adsorption process

Jie Ye[a,b,c], Xiangna Cong[d], Panyue Zhang[a,b,*], Erhard Hoffmann[c,*], Guangming Zeng[a,b], Yang Liu[a,b], Wei Fang[a,b], Yan Wu[a,b], Haibo Zhang[a,b]

[a] College of Environmental Science and Engineering, Hunan University, Changsha 410082, PR China
[b] Key Laboratory of Environmental Biology and Pollution Control (Hunan University), Ministry of Education, Changsha 410082, PR China
[c] Department of Aquatic Environmental Engineering, Karlsruhe Institute of Technology, Karlsruhe D-76131, Germany
[d] The Institute for Applied Materials IAM-WK, Karlsruhe Institute of Technology, Karlsruhe D-76131, Germany

ARTICLE INFO

Article history:
Received 14 June 2015
Received in revised form 5 August 2015
Accepted 6 August 2015
Available online 10 August 2015

Keywords:
Red mud
Phosphate complex
Precipitation
Ion exchange
Surface deposition

ABSTRACT

Acid-activated neutralized red mud (AaN-RM) has become a promising adsorbent for phosphate adsorption. The maximum phosphate adsorption capacity of AaN-RM reached 492.46 mg g^{-1} in this study, which was much higher than that of many other adsorbents. However, no study has specifically investigated how the phosphate reacted with AaN-RM. For the first time the interaction between phosphate and AaN-RM during adsorption process was investigated in this research. Kinetic models and isotherms were used to analyze the possible reaction pathways between AaN-RM and phosphate. Particularly, the phosphate complexes on AaN-RM surface, and the exact role of different adsorption mechanisms were systemically identified. The phosphate adsorption was well described by pseudo second-order kinetic model and Langmuir–Freundlich isotherm, which suggested that chemisorption occurred between the phosphate and AaN-RM, and the phosphate adsorption was governed by heterogeneous processes. Furthermore, the phosphate complexes of Fe–P, Al–P, Fe–P–H_3PO_4 and Al–P–H_3PO_4 were formed on AaN-RM surface through ion exchange, precipitation and surface deposition mechanisms. XPS analysis of P 2p peak showed that 59.78% of the phosphate was adsorbed through the ion exchange and precipitation with strong chemical bonds, and 40.22% was adsorbed through the surface deposition with weak chemical bonds.

1. Introduction

Red mud, a waste tailing generated after alumina producing process, is a kind of highly alkaline slurry [1]. The amount of red mud ranges from 0.3 to more than two tons per ton of alumina production. The global production of red mud was about 120 million tons per year [2]. Currently, most red mud is stored in impoundments, which results in serious environmental pollution and risk [3]. Therefore, it is necessary to find alternative options for red mud treatment and utilization.

The application of red mud is usually restricted by its caustic nature caused by the use of caustic soda and lime in alumina extraction. Several neutralizing techniques have been employed to decrease the alkalinity of red mud and use the modified red mud as absorbent, including neutralization with CO_2, seawater and combination of them [4]. The neutralization effectively increased the variety of ionic binding and improved the adsorption performance of red mud [5]. For instance, Genç et al. [6] illustrated that seawater-neutralized red mud more efficiently removed As(V) than unneutralized red mud. Cengeloglu et al. [7] found that distilled water-neutralized red mud can be used as an effective adsorbent for boron removal in a wide pH range of 2–7. Sahu et al. [8] investigated the potential of CO_2-neutralized red mud for the adsorption of Zn(II) ions from aqueous solution, and found that the maximum adsorption capacity of CO_2-neutralized red mud reached 14.92 mg g^{-1}. In recent years, acid activation after neutralization of red mud has been proven to be effective for further improving the physicochemical characters of red mud. Genç-Fuhrman et al. [9,10] demonstrated that acid-activated neutralized red mud (AaN-RM) had good adsorption potential for arsenate removal in the batch and fixed-bed studies. Tor et al. [11] investigated the possibility of increasing the phenol adsorption capacity of neutralized red mud

* Corresponding authors at: College of Environmental Science and Engineering, Hunan University, Yuelushan, Changsha 410082, China.
E-mail addresses: eyejie@126.com (J. Ye), Xiangnacong@hotmail.com (X. Cong), zhangpanyue@hnu.edu.cn (P. Zhang), erhard.hoffmann@kit.edu (E. Hoffmann), zgming@hnu.edu.cn (G. Zeng), jungsten@163.com (Y. Liu), fw8905@163.com (W. Fang), wuyan19850827@hotmail.com (Y. Wu), haibo_zhang@hnu.edu.cn (H. Zhang).

http://dx.doi.org/10.1016/j.apsusc.2015.08.053
0169-4332/

by acid treatment, and the phenol adsorption capacity significantly increased after acid activation. In our previous paper, AaN-RM was successfully prepared and used for effective phosphate adsorption [12].

In order to better design and control the phosphate adsorption onto AaN-RM, it is necessary to understand the adsorption mechanisms involved. However, previous studies mainly focused on the improvement of phosphate adsorption capacity of AaN-RM. No study has systemically investigated how the phosphate reacted with AaN-RM. Akhurst et al. [13] suggested that chemisorption could be important during phosphate adsorption by AaN-RM. The functional species on AaN-RM surface, which were responsible for the chemisorption, have not been identified. Genç-Fuhrman et al. [9] attributed the excellent adsorption performance of AaN-RM to the increased surface area by cleaning of adsorption sites during acid activation. However, Freire et al. [14] concluded that the increased surface area was more likely attributed to the generation of amorphous and semi-amorphous Al and Fe. There are no sufficient evidences to reveal the governing mechanisms for phosphate adsorption, and the exact phosphate complexes on AaN-RM surface are unclear.

Therefore, the specific objectives of this study were: (1) to analyze the possible reaction pathways between AaN-RM and phosphate using different kinetic models and isotherms; (2) to identify the form of phosphate complexes on AaN-RM surface, and to analyze the exact role of different phosphate adsorption mechanisms.

2. Materials and methods

2.1. Materials

The red mud was provided by Shandong Aluminum Industry Corporation (Zibo, China), and the preparation method of AaN-RM can be found in [12]. The phosphate solution was prepared by potassium dihydrogen phosphate, which was of analytical grade (Merck, Germany).

2.2. Adsorption studies

According to the preliminary experiments with one-factor-at-a-time method, the initial solution pH and adsorption temperature were the important operational factors influencing the phosphate adsorption onto AaN-RM. Further preliminary experiments using response surface methodology (RSM) with central composite design (CCD) confirmed that a maximum predicted phosphate adsorption capacity was achieved at an initial solution pH of 4.19 and an adsorption temperature of 52.18 °C. For operation convenience, in this research the initial solution pH and adsorption temperature were chosen as 4.5 and 50 °C, respectively.

Adsorption kinetic experiments were conducted in beaker flasks containing 200 mg L^{-1} phosphate solution with an AaN-RM dose of 0.5 g L^{-1}. The flasks were shaken at 100 r min^{-1}, and the samples were taken at predetermined time intervals for the analysis of residual phosphate concentration. The adsorption temperature was controlled with a gyratory water bath shaker (model G76, New Brunswick Scientific, USA).

Adsorption isotherm experiments were conducted in beaker flasks containing different phosphate solutions (50, 100, 200, 400, 1000 mg L^{-1}) with an AaN-RM dose of 0.5 g L^{-1}. The flasks were shaken at 100 r min^{-1} until adsorption equilibrium. After equilibrium, the samples were centrifuged and the residual phosphate concentration was analyzed.

The phosphate concentration was determined via the spectrophotometric method DIN-EN-ISO-15681-1 with a QuikChem 8500 flow injection analysis system (Lachat Instruments, USA). The pH value was measured with a multimeter (model Multiline P4, WTW, Germany). All experiments were conducted in triplicate, and the average values were used for data analysis.

2.3. Adsorption kinetic models and isotherms

Three kinetic models including pseudo first-order model, Elovich model and pseudo second-order model were examined. The governing equations are as Eqs. (1)–(3) [15–17]:

$$\frac{dq_t}{dt} = k_1(q_e - q_t) \quad \text{Pseudo first-order} \tag{1}$$

$$\frac{dq_t}{dt} = \alpha e^{-\beta q_t} \quad \text{Elovich} \tag{2}$$

$$\frac{dq_t}{dt} = k_2(q_e - q_t)^2 \quad \text{Pseudo second-order} \tag{3}$$

where q_e (mg g^{-1}) is the adsorption capacity of sample at equilibrium, q_t (mg g^{-1}) is the adsorption capacity of sample at time t (min), k_1 (min^{-1}) and k_2 (g mg^{-1} min^{-1}) are the equilibrium rate constants for pseudo first-order and pseudo second-order kinetics, α (mg g^{-1} min^{-1}) and β (g mg^{-1}) are the Elovich constants.

Three common types of isotherms, Langmuir isotherm, Freundlich isotherm and Langmuir–Freundlich isotherm, were applied to describe the equilibrium adsorption. The governing equations are shown as Eqs. (4)–(6) [18–20]:

$$q_e = \frac{K_L q_{max} C_e}{1 + k_L C_e} \quad \text{Langmuir} \tag{4}$$

$$q_e = K_F C_e^n \quad \text{Freundlich} \tag{5}$$

$$q_e = \frac{K_{LF} q_{max} {C_e}^n}{1 + K_{LF} {C_e}^n} \quad \text{Langmuir–Freundlich} \tag{6}$$

where C_e (mg L^{-1}) is the equilibrium concentration, q_e (mg g^{-1}) is the adsorption capacity of sample at equilibrium, q_{max} (mg g^{-1}) is the maximum adsorption capacity of sample, K_L (L mg^{-1}) represents the Langmuir bonding term related to interaction energies, K_F ($mg^{(1-n)}$ L^n g^{-1}) is the Freundlich affinity coefficient, n (dimensionless) is the Freundlich linearity constant, and K_{LF} (L^n mg^{-n}) represents the Langmuir–Freundlich affinity parameter.

2.4. Mechanism analysis

AaN-RM samples before and after phosphate adsorption were characterized for further mechanism analysis. AaN-RM after phosphate adsorption was collected from isotherm studies with an initial phosphate concentration of 200 mg L^{-1}, followed by rinsing with deionized water and drying at 50 °C.

Sequential extraction method, proposed by European commission (BCR-684), was used to study the chemical forms of phosphate bound to AaN-RM [21]. The chemical composition of AaN-RM was determined by X-Ray Fluorescence Spectrometer (S4 Explorer, Bruker, Germany). The specific surface area and pore size distribution of AaN-RM were obtained by nitrogen gas sorption method (ASAP 2020 V3.04 H, Micromeritics, USA). The surface structure and element composition of AaN-RM were analyzed with an electron dispersive X-ray analysis (OXFORD X-Max, Oxford Instruments, UK), which was coupled with an electronic detector (LEO 1530, LEO, Germany). The XRD pattern of AaN-RM was detected using an X-ray diffractometer (XRD-6000, Shimadzu, Japan) with Cu Kα radiation at 40 kV and 30 mA, and recorded in a 2θ range of 10–70° at a scan speed range of 0.02° s^{-1}. Fourier transform infrared (FTIR) spectrum of AaN-RM was recorded at room temperature using a FTIR Spectrometer (MAGNA FTIR 750, Nicolet, USA) in 500–4000 cm^{-1} region. The KBr (FTIR grade, Fluka) was dried at 200 °C for 24 h.

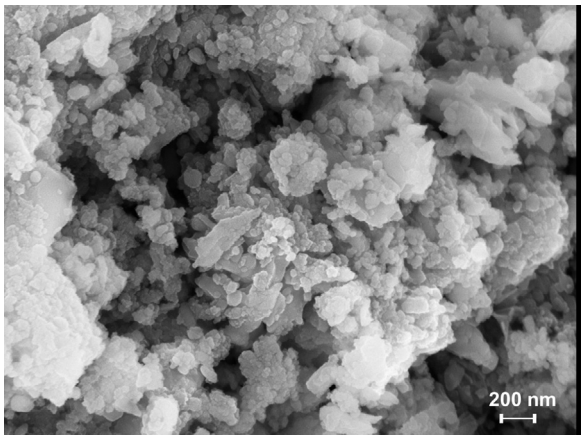

Fig. 1. SEM image of AaN-RM before phosphate adsorption.

X-ray photoelectron spectroscopy (XPS) measurement was performed using an X-ray photoelectron spectrometer (Escalab 250Xi, Thermo Scientific, UK) equipped with Al Kα radiation (1486.6 eV) to determine the elemental composition on sample surface, and the distribution of different elemental compositions was calculated from the area under corresponding curves.

3. Results and discussion

3.1. Characterization of AaN-RM

The SEM image of AaN-RM before phosphate adsorption was shown in Fig. 1. AaN-RM surface was rough with lots of pores. According to the BET test, the AaN-RM displayed a larger BET surface area of 80.63 $m^2\ g^{-1}$ than neutralized red mud (40.67 $m^2\ g^{-1}$). The increased surface area might be attributed to the generation of amorphous and semi-amorphous materials of Fe and Al after acid activation, because Fe and Al were the main components of AaN-RM (as shown in Table 1). Moreover, the Al content in AaN-RM increased substantially after acid activation.

3.2. Adsorption kinetics and isotherms

Kinetic studies not only help to predict the reaction rate but also provide the understanding on reaction pathways in order to design appropriate adsorption systems. Kinetic data for the phosphate adsorption onto AaN-RM is shown in Fig. 2. The phosphate adsorption occurred very rapidly. 90.88% of the phosphate was adsorbed within 5 min, and then followed a slow process until adsorption equilibrium. The sufficient adsorption sites on AaN-RM surface and the available driving force for mass transfer might be provided at the initial stage of adsorption. The kinetic parameters for pseudo

Table 1
Chemical composition of neutralized red mud and AaN-RM.

Constituent	Neutralized red mud (wt.%)	AaN-RM (wt.%)
Fe_2O_3	47.13	33.88
Al_2O_3	23.62	30.96
Na_2O	8.35	3.83
SiO_2	9.12	15.52
TiO_2	7.51	14.69
CaO	2.38	0.54
Cr_2O_3	0.17	0.22
MnO	0.14	0.06
K_2O	0.05	0.10
CuO	0.03	0.01
NiO	0.01	0.02
MgO	1.49	0.17

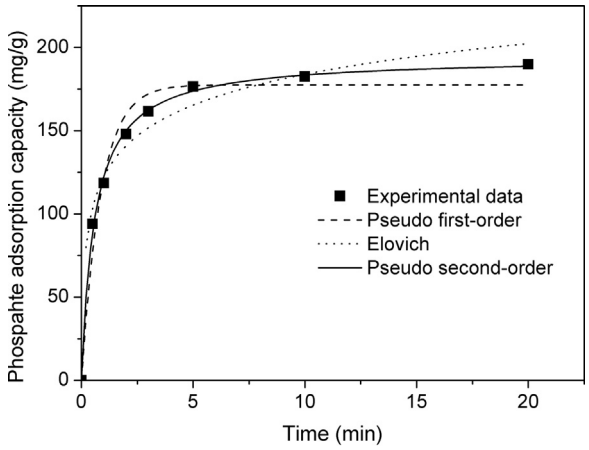

Fig. 2. Adsorption kinetics of phosphate adsorption onto AaN-RM (AaN-RM dosage: 0.5 g L^{-1}; initial phosphate concentration: 200 mg L^{-1}; initial solution pH: 4.5; adsorption temperature: 50 °C; agitation speed: 100 r min^{-1}).

Table 2
Parameters of kinetic models for phosphate adsorption onto AaN-RM (AaN-RM dosage: 0.5 g L^{-1}; initial phosphate concentration: 200 mg L^{-1}; initial solution pH: 4.5; adsorption temperature: 50 °C; agitation speed: 100 r min^{-1}).

	Parameter 1	Parameter 2	R^2
Pseudo first-order	k_1 = 2.668 min^{-1}	q_e = 177.60 mg g^{-1}	0.971
Elovich	α = 2.64E+3 mg g^{-1} min^{-1}	β = 0.038 g mg^{-1}	0.978
Pseudo second-order	k_2 = 0.009 g mg^{-1} min^{-1}	q_e = 194.21 mg g^{-1}	0.998

first-order, Elovich and pseudo second-order models are given in Table 2. According to correlation coefficient R^2, the pseudo second-order model fitted the adsorption process better than Elovich model and pseudo first-order model. The pseudo second-order expression is derived based on the supposition of chemisorption [22,23], therefore, the chemisorption might occur between the phosphate and AaN-RM.

Adsorption isotherm is fundamental for describing the interactive behaviors between absorbate and adsorbent, which can directly illustrate and compare the adsorption performance between different adsorbents. This information is crucial for adsorbent selection [24]. As shown in Fig. 3, the Langmuir–Freundlich model fitted the isotherm data better than the Langmuir model and Freundlich model with a correlation coefficient (R^2) of 0.998 (Table 3), which might be attributed to the uneven surface

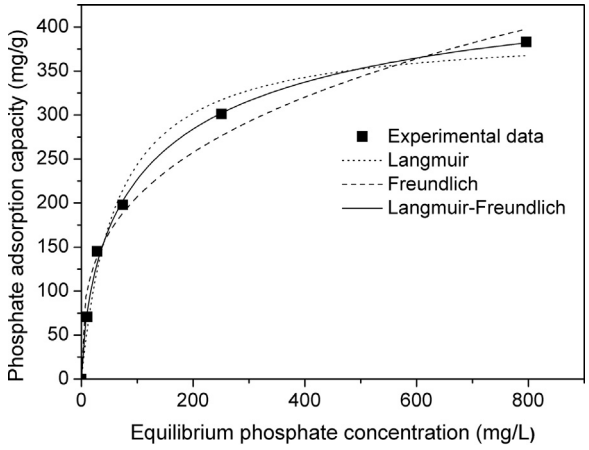

Fig. 3. Isotherm models for phosphate adsorption onto AaN-RM (AaN-RM dosage: 0.5 g L^{-1}; initial phosphate concentration: 50, 100, 200, 400, 1000 mg L^{-1}; initial solution pH: 4.5; adsorption temperature: 50 °C; agitation speed: 100 r min^{-1}).

Table 3
Parameters of adsorption isotherms for phosphate adsorption onto AaN-RM (AaN-RM dosage: 0.5 g L^{-1}; initial phosphate concentration: 50, 100, 200, 400, 1000 mg L^{-1}; initial solution pH: 4.5; adsorption temperature: 50 °C; agitation speed: 100 r min^{-1}).

	Parameter 1	Parameter 2	Parameter 3	R^2
Langmuir	K_L = 0.016 L mg^{-1}	q_{max} = 396.355 mg g^{-1}		0.983
Freundlich	K_F = 48.580 $mg^{(1-n)}$ L^n g^{-1}	n = 0.315		0.975
Langmuir–Freundlich	K_{LF} = 0.038 L^n mg^{-n}	q_{max} = 492.464 mg g^{-1}	n = 0.674	0.996

Table 4
Summary of the maximum phosphate adsorption capacity of different adsorbents.

Adsorbent	Isotherm	Maximum phosphate adsorption capacity (mg g^{-1})	Literatures
La(III)-modified bentonite	Langmuir	14.0	[26]
Amorphous zirconium oxide nanoparticles	Langmuir	99.01	[27]
Lanthanum hydroxide-doped activated carbon fiber	Langmuir	15.3	[28]
Iron hydroxide-eggshell waste	Langmuir	14.49	[29]
Engineered biochar	Langmuir–Freundlich	103.8	[30]
Digested sugar beet tailing biochar	Langmuir–Freundlich	0.71	[25]
AaN-RM	Langmuir–Freundlich	492.46	This work

of AaN-RM (as shown in Fig. 1). The analysis of pore size distribution of AaN-RM illustrated that a large amount of micropores (12.94 m^2 g^{-1}) and mesopores (67.69 m^2 g^{-1}) was formed on the surface of AaN-RM. The interaction between phosphate and AaN-RM could be affected by heterogeneous process. Therefore, the heterogeneous Langmuir–Freundlich isotherm better described the adsorption data than Langmuir and Freundlich isotherms [25]. The maximum capacity of AaN-RM calculated from Langmuir–Freundlich isotherm reached 492.46 mg g^{-1} (Table 3), which was much higher than that of many other adsorbents for phosphate adsorption (Table 4). The mineralogical changes and increased quantities of amorphous precipitates after acid activation might increase the specific surface area, and then substantially improved the phosphate adsorption capacity of AaN-RM [14]. Furthermore, many of the primary minerals presented as very fine grain in AaN-RM, and typically 80% of AaN-RM particles were smaller than 2 μm. The very fine grain size also provided excellent phosphate adsorption capacity of AaN-RM [31]. So the AaN-RM is a promising phosphate adsorbent in commercial application.

3.3. Formation of phosphate complexes

The EDX spectra of AaN-RM are shown in Fig. 4. Compared with AaN-RM before phosphate adsorption, a clear signal of phosphorus (P) was observed in the EDX spectrum of AaN-RM after phosphate adsorption, which demonstrated that the phosphate was successfully adsorbed onto AaN-RM surface.

Sequential extraction method was used to study the chemical forms of phosphate bound to AaN-RM. The content of total phosphorus extracted by BCR-684 was 183.5 ± 1.12 mg g^{-1}, which was close to the total phosphorus adsorbed onto the AaN-RM (190 ± 2.89 mg g^{-1}). Because the phosphorus in this research mainly came from the KH_2PO_4 in wastewater, the content of inorganic phosphorus extracted by BCR-684 was 183.00 ± 0.19 mg g^{-1}, which was much higher than that of organic phosphorus (1.93 ± 0.28 mg g^{-1}). Additionally, the phosphorus bounded with Fe and Al (Fe–P and Al–P) reached 181.30 ± 4.54 mg g^{-1}, which was much higher than that associated with Ca and Mg (1.44 ± 0.23 mg g^{-1}). Therefore, Fe–P

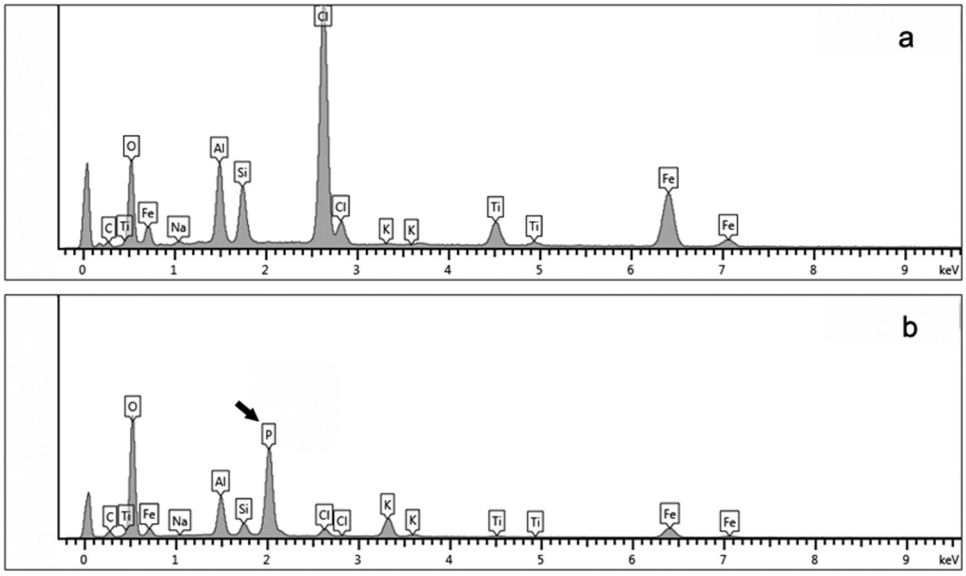

Fig. 4. EDX spectra of AaN-RM before phosphate adsorption (a) and after phosphate adsorption (b).

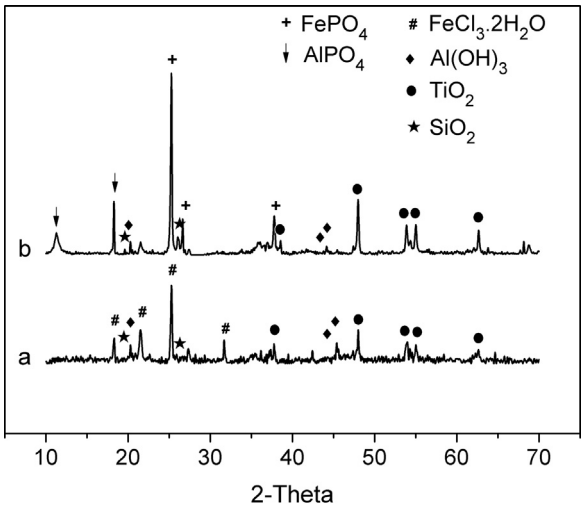

Fig. 5. XRD patterns of AaN-RM before phosphate adsorption (a) and after phosphate adsorption (b).

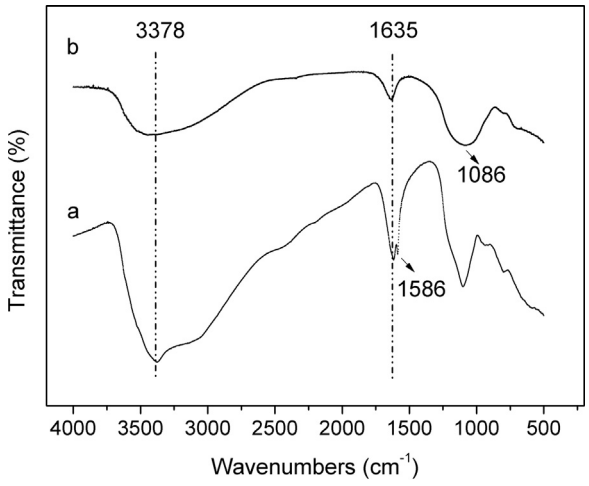

Fig. 6. FTIR spectra of AaN-RM before phosphate adsorption (a) and after phosphate adsorption (b).

or/and Al–P was the main forms of inorganic phosphorus, and played an important role during phosphate adsorption onto AaN-RM.

Fig. 5 shows X-ray diffraction patterns of AaN-RM. The AaN-RM before phosphate adsorption had specific chemical composition diffraction peaks at different 2θ (°), indicating the presence of iron chloride hydrate ($FeCl_3{\cdot}2H_2O$), Gibbsite ($Al(OH)_3$), Anatase (TiO_2) and Quartz (SiO_2). The peak of $FeCl_3{\cdot}2H_2O$ disappeared after phosphate adsorption. Simultaneously, sharp and intense peaks of $FePO_4$ were observed. The phosphate easily reacted with $FeCl_3{\cdot}2H_2O$ by the precipitation mechanism to form strong chemical bonds. Hsu [32] also demonstrated that the affinity of Fe^{3+} for phosphate was strong enough to form $FePO_4$ precipitate. Therefore, the Fe–P was an important phosphate complex, and the precipitation was an important mechanism for the phosphate adsorption onto AaN-RM.

The phosphates can also form chemisorbed complexes via ligand exchange reactions with hydroxide. Atkinson et al. [33] proposed that the hydrolysis of Fe^{3+} could form Fe–OH on the surface of goethite crystals, and then phosphate specifically replaced hydroxyl group and formed bridges between adjacent Fe^{3+}. Kim et al. [34] demonstrated that the phosphate ions could bind to Fe^{3+} through two P–O–Fe linkages. Wang et al. [35] concluded that the chemisorbed phosphate complexes could be formed via ligand exchange reaction between phosphate oxygens and hydroxyl oxygens of Fe–OH. Therefore, ion exchange was also an important mechanism for the formation of Fe–P complex.

The FTIR spectra of AaN-RM are shown in Fig. 6. For all samples, a strong and broad band at 3600–3100 cm^{-1} region (O–H stretching vibration) should be assigned for the presence of hydroxyl of coordinate water molecules [36–38]. Compared with the spectrum of AaN-RM before phosphate adsorption, the band at 1635 cm^{-1} (O–H bending vibration) dramatically weakened, and the band at 1586 cm^{-1} (O–H bending vibration) completely disappeared after phosphate adsorption [39]. Meanwhile, a new peak at 1086 cm^{-1} was observed, which should be assigned to P–O [40]. The results suggested that the adsorption mechanism may result from the ion exchange reaction between the hydroxyl of $Al(OH)_3$ and phosphate in solution, because the $Al(OH)_3$ was the main hydroxide on AaN-RM surface (shown in Fig. 5), and the peaks of $Al(OH)_3$ disappeared after phosphate adsorption. Therefore, Al–P was another main phosphate complex during phosphate adsorption onto AaN-RM. With the initial solution pH of 4.5, $H_2PO_4^-$ was the main existence form of phosphate in the solution. Therefore, the adsorption process could be described by Eq. (7) [41]:

$$2{\equiv}Al{-}OH + H_2PO_4^- \leftrightharpoons ({\equiv}Al)_2HPO_4 + H_2O + OH^- \quad (7)$$

where symbol ≡denotes the AaN-RM surface.

As shown in Fig. 5, sharp and intense peaks of $AlPO_4$ were also observed after phosphate adsorption. Therefore, we could conclude that the $Al(OH)_3$ reacted with phosphate by the precipitation mechanism. The result was consistent with that from Veith and Sposito [42], who proposed that the precipitate formed during the phosphate adsorption onto $Al(OH)_3$ was an amorphous analog of variscite. Lookman et al. [43] found the formation of an amorphous aluminum phosphate phase on the $Al(OH)_3$ surface through ^{27}Al and ^{31}P solid-state MAS NMR.

Van Emmerik et al. [44] found that the phosphate could bind to the formed phosphate complexes. Similarly, Chusuei et al. [45] demonstrated that hydrogen bonding was involved in the formation of additional phosphate overlayer until the adsorption saturation. This meant that the formed Fe–P and Al–P on AaN-RM surface could further adsorb additional phosphate by surface deposition mechanism (hydrogen bonding) to form new phosphate complexes Fe–P–H_3PO_4 and Al–P–H_3PO_4. Because the phosphate adsorption process by Fe–P and Al–P with surface deposition mechanism was reversible, the final phosphate complexes formed included Fe–P, Al–P, Fe–P–H_3PO_4 and Al–P–H_3PO_4.

Illustration scheme of the phosphate adsorption onto AaN-RM can be shown in Fig. 7. The $FeCl_3{\cdot}2H_2O$ and $Al(OH)_3$ reacted with $H_2PO_4^-$ by ion exchange and precipitation mechanisms to form Fe–P and Al–P. Then the Fe–P and Al–P further adsorbed additional phosphate to form new phosphate complexes of Fe–P–H_3PO_4 and Al–P–H_3PO_4 with surface deposition mechanism.

3.4. Exact role of different adsorption mechanisms

XPS spectra of P 2p region for AaN-RM after phosphate adsorption are shown in Fig. 8. The binding energies of P 2p peak represented two kinds of phosphate species. The binding energy at 134.2 eV corresponded to $H_2PO_4^-$ [46], which demonstrated the reaction of $H_2PO_4^-$ with $FeCl_3{\cdot}2H_2O$ and $Al(OH)_3$ by ion exchange and precipitation mechanisms. Another intense compound at a lower binding energy of 133.4 eV was associated with H_3PO_4 analog, and the phosphate adsorption mechanism was surface deposition [30]. The areas under the corresponding curves for XPS analysis indicated that 59.78% of the phosphate was adsorbed onto AaN-RM through the ion exchange and precipitation with strong

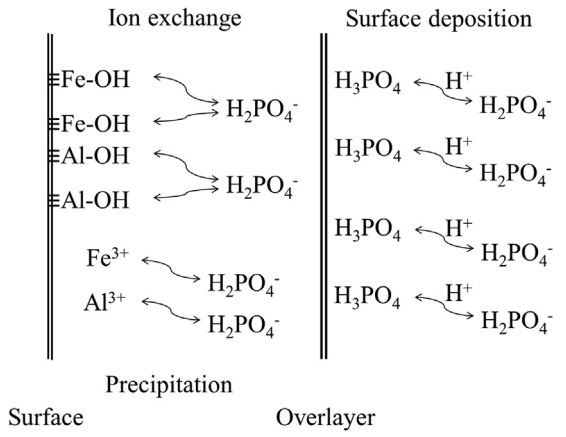

Fig. 7. Illustration scheme of the phosphate adsorption onto AaN-RM.

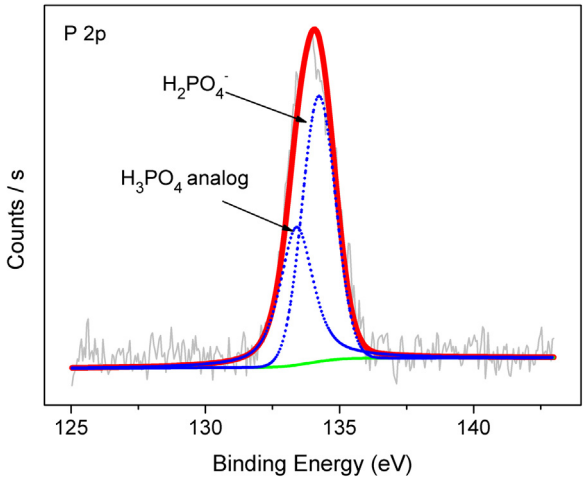

Fig. 8. XPS spectra of P 2p region for AaN-RM after phosphate adsorption.

chemical bonds, and 40.22% was adsorbed through the surface deposition with weak chemical bonds.

4. Conclusion

(1) The maximum capacity of AaN-RM reached 492.46 mg g^{-1} in this study, which was much higher than that of many other adsorbents. The phosphate adsorption process was well described by pseudo second-order kinetic model, illustrating that chemisorption occurred between the phosphate and AaN-RM.

(2) Langmuir–Freundlich isotherm matched the experimental data better than Langmuir isotherm and Freundlich isotherm, which demonstrated that the phosphate adsorption was governed by heterogeneous processes.

(3) Mechanism analyses demonstrated that the $FeCl_3{\cdot}2H_2O$ and $Al(OH)_3$ could react with $H_2PO_4^-$ by ion exchange and precipitation mechanisms to form Fe–P and Al–P, respectively. Then the Fe–P and Al–P further adsorbed additional phosphate to form new phosphate complexes of Fe–P–H_3PO_4 and Al–P–H_3PO_4 with surface deposition mechanism.

(4) XPS analysis of P 2p peak on AaN-RM after phosphate adsorption demonstrated that 59.78% of the phosphate was adsorbed through the ion exchange and precipitation with strong chemical bonds, and 40.22% was adsorbed through the surface deposition with weak chemical bonds.

Acknowledgements

The authors are thankful to the CSC (China Scholarship Council), the National Natural Science Foundation of China (51178047, 51378190, 51039001), and Furong Scholar of Hunan Province for support.

References

[1] C. Brunori, C. Cremisini, P. Massanisso, V. Pinto, L. Torricelli, Reuse of a treated red mud bauxite waste: studies on environmental compatibility, J. Hazard. Mater. 117 (2005) 55–63.
[2] Q. Yue, Y. Zhao, Q. Li, W. Li, B. Gao, S. Han, Y. Qi, H. Yu, Research on the characteristics of red mud granular adsorbents (RMGA) for phosphate removal, J. Hazard. Mater. 176 (2010) 741–748.
[3] S. Wang, Y. Boyjoo, A. Choueib, Z.H. Zhu, Removal of dyes from aqueous solution using fly ash and red mud, Water Res. 39 (2005) 129–138.
[4] L.M. Despland, M.W. Clark, M. Aragno, T. Vancov, Minimising alkalinity and pH spikes from Portland cement-bound Bauxsol (seawater-neutralized red mud) pellets for pH circum-neutral waters, Environ. Sci. Technol. 44 (2010) 2119–2125.
[5] R.C. Sahu, R.K. Patel, B.C. Ray, Neutralization of red mud using CO_2 sequestration cycle, J. Hazard. Mater. 179 (2010) 28–34.
[6] H. Genç, J.C. Tjell, D. McConchie, O. Schuiling, Adsorption of arsenate from water using neutralized red mud, J. Colloid Interface Sci. 264 (2003) 327–334.
[7] Y. Cengeloglu, A. Tor, G. Arslan, M. Ersoz, S. Gezgin, Removal of boron from aqueous solution by using neutralized red mud, J. Hazard. Mater. 142 (2007) 412–417.
[8] R.C. Sahu, R. Patel, B.C. Ray, Adsorption of Zn(II) on activated red mud: neutralized by CO_2, Desalination 266 (2011) 93–97.
[9] H. Genç-Fuhrman, J.C. Tjell, D. McConchie, Increasing the arsenate adsorption capacity of neutralized red mud (Bauxsol), J. Colloid Interface Sci. 271 (2004) 313–320.
[10] H. Genç-Fuhrman, H. Bregnhøj, D. McConchie, Arsenate removal from water using sand–red mud columns, Water Res. 39 (2005) 2944–2954.
[11] A. Tor, Y. Cengeloglu, M. Ersoz, Increasing the phenol adsorption capacity of neutralized red mud by application of acid activation procedure, Desalination 242 (2009) 19–28.
[12] J. Ye, P. Zhang, E. Hoffmann, G. Zeng, Y. Tang, J. Dresely, Y. Liu, Comparison of response surface methodology and artificial neural network in optimization and prediction of acid activation of Bauxsol for phosphorus adsorption, Water Air Soil Pollut. 225 (2014) 2225.
[13] D.J. Akhurst, G.B. Jones, M. Clark, D. McConchie, Phosphate removal from aqueous solutions using neutralised bauxite refinery residues (Bauxsol™), Environ. Chem. 3 (2006) 65–74.
[14] T.S.S. Freire, M.W. Clark, M.J. Comarmond, T.E. Payne, A.J. Reichelt-Brushett, G.J. Thorogood, Electroacoustic isoelectric point determinations of bauxite refinery residues: different neutralisation techniques and minor mineral effects, Langmuir 28 (2012) 11802–11811.
[15] R.S. Juang, M.L. Chen, Application of the Elovich equation to the kinetics of metal sorption with solvent-impregnated resins, Ind. Eng. Chem. Res. 36 (1997) 813–820.
[16] W.J. Weber, J.C. Morris, Advances in water pollution research: removal of biologically resistant pollutant from waste water by adsorption, in: Proceedings of 1st International Conference on Water Pollution Symposium, vol. 2, 1962, pp. 231–266.
[17] J. Youngran, M. Fan, J.V. Leeuwen, J.F. Belczyk, Effect of competing solutes on arsenic(V) adsorption using iron and aluminum oxides, J. Environ. Sci. 19 (2007) 910–919.
[18] J.L. Gong, B. Wang, G.M. Zeng, C.P. Yang, C.G. Niu, Q.Y. Niu, W.J. Zhou, Y. Liang, Removal of cationic dyes from aqueous solution using magnetic multi-wall carbon nanotube nanocomposite as adsorbent, J. Hazard. Mater. 164 (2009) 1517–1522.
[19] I. Langmuir, The adsorption of gases on plane surfaces of glass, mica and platinum, J. Am. Chem. Soc. 40 (1918) 1361–1403.
[20] K.R. Hall, L.C. Eagleton, A. Acrivos, T. Vermeulen, Pore- and solid-diffusion kinetics in fixed-bed adsorption under constant pattern conditions, Ind. Eng. Chem. Fundam. 5 (1966) 212–223.
[21] V. Ruban, G. Rauret, European Commission BCR Information Report, European Commission, 2001.
[22] X. Hu, J. Wang, Y. Liu, X. Li, G. Zeng, Z. Bao, X. Zeng, A. Chen, F. Long, Adsorption of chromium (VI) by ethylenediamine-modified cross-linked magnetic chitosan resin: isotherms, kinetics and thermodynamics, J. Hazard. Mater. 185 (2011) 306–314.
[23] Y. Sun, G. Zhou, X. Xiong, X. Guan, L. Li, H. Bao, Enhanced arsenite removal from water by $Ti(SO_4)_2$ coagulation, Water Res. 47 (2013) 4340–4348.
[24] X. Dou, D. Mohan, C.U. Pittman, Arsenate adsorption on three types of granular schwertmannite, Water Res. 47 (2013) 2938–2948.
[25] Y. Yao, B. Gao, M. Inyang, A.R. Zimmerman, X. Cao, P. Pullammanappallil, L. Yang, Removal of phosphate from aqueous solution by biochar derived from anaerobically digested sugar beet tailings, J. Hazard. Mater. 190 (2011) 501–507.

[26] V. Kuroki, G.E. Bosco, P.S. Fadini, A.A. Mozeto, A.R. Cestari, W.A. Carvalho, Use of a La (III)-modified bentonite for effective phosphate removal from aqueous media, J. Hazard. Mater. 274 (2014) 124–131.
[27] Y. Su, H. Cui, Q. Li, S. Gao, J.K. Shang, Strong adsorption of phosphate by amorphous zirconium oxide nanoparticles, Water Res. 47 (2013) 5018–5026.
[28] L. Zhang, Q. Zhou, J. Liu, N. Chang, L. Wan, J. Chen, Phosphate adsorption on lanthanum hydroxide-doped activated carbon fiber, Chem. Eng. J. 185 (2012) 160–167.
[29] N.Y. Mezenner, A. Bensmaili, Kinetics and thermodynamic study of phosphate adsorption on iron hydroxide-eggshell waste, Chem. Eng. J. 147 (2009) 87–96.
[30] Y. Yao, B. Gao, J. Chen, L. Yang, Engineered biochar reclaiming phosphate from aqueous solutions: mechanisms and potential application as a slow-release fertilizer, Environ. Sci. Technol. 47 (2013) 8700–8708.
[31] M. Gräfe, G. Power, C. Klauber, Bauxite residue issues: III. Alkalinity and associated chemistry, Hydrometallurgy 108 (2011) 60–79.
[32] P.H. Hsu, Comparison of iron (III) and aluminum in precipitation of phosphate from solution, Water Res. 10 (1976) 903–907.
[33] R.J. Atkinson, A.M. Posner, J.P. Quirk, Kinetics of isotopic exchange of phosphate at the α-FeOOH-aqueous solution interface, J. Inorg. Nucl. Chem. 34 (1972) 2201–2211.
[34] J. Kim, W. Li, B.L. Philips, C.P. Grey, Phosphate adsorption on the iron oxyhydroxides goethite, akaganeite, and lepidocrocite: a 31P NMR study, Energy Environ. Sci. 4 (2011) 4298–4305.
[35] L. Wang, C.V. Putnis, E. Ruiz-Agudo, J. Hövelmann, A. Putnis, In situ imaging of interfacial precipitation of phosphate on goethite, Environ. Sci. Technol. 49 (2015) 4184–4192.
[36] L. Lijklema, Interaction of orthophosphate with iron (III) and aluminum hydroxides, Environ. Sci. Technol. 14 (1980) 537–541.
[37] P. Xu, G.M. Zeng, D.L. Huang, C.L. Feng, S. Hu, M.H. Zhao, C. Lai, Z. Wei, C. Huang, G.X. Xie, Z.F. Liu, Use of iron oxide nanomaterials in wastewater treatment: a review, Sci. Total Environ. 424 (2012) 1–10.
[38] J. Zhou, S. Yang, J. Yu, Z. Shu, Novel hollow microspheres of hierarchical zinc–aluminum layered double hydroxides and their enhanced adsorption capacity for phosphate in water, J. Hazard. Mater. 192 (2011) 1114–1121.
[39] F. Long, J.L. Gong, G.M. Zeng, L. Chen, X. Wang, J. Deng, Q. Niu, H. Zhang, X. Zhang, Removal of phosphate from aqueous solution by magnetic Fe–Zr binary oxide, Chem. Eng. J. 171 (2011) 448–455.
[40] M.C. Zenobi, C.V. Luengo, M.J. Avena, E.H. Rueda, An ATR-FTIR study of different phosphonic acids adsorbed onto boehmite, Spectrochim. Acta A 75 (2010) 1283–1288.
[41] Y. Yang, Y.Q. Zhao, A.O. Babatunde, L. Wang, Y.X. Ren, Y. Han, Characteristics and mechanisms of phosphate adsorption on dewatered alum sludge, Sep. Purif. Technol. 51 (2006) 193–200.
[42] J.A. Veith, G. Sposito, Reactions of aluminosilicates, aluminum hydrous oxides, and aluminum oxide with o-phosphate: the formation of X-ray amorphous analogs of variscite and montebrasite, Soil Sci. Soc. Am. J. 41 (1977) 870–876.
[43] R. Lookman, P. Grobet, R. Merckx, K. Vlassak, Phosphate sorption by synthetic amorphous aluminum hydroxides: a 27Al and 31P solid-state MAS NMR spectroscopy study, Eur. J. Soil Sci. 45 (1994) 37–44.
[44] T.J. Van Emmerik, D.E. Sandström, O.N. Antzutkin, M.J. Angove, B.B. Johnson, ^{31}P solid-state nuclear magnetic resonance study of the sorption of phosphate onto gibbsite and kaolinite, Langmuir 23 (2007) 3205–3213.
[45] C.C. Chusuei, D.W. Goodman, M.J. Van Stipdonk, D.R. Justes, K.H. Loh, E.A. Schweikert, Solid–liquid adsorption of calcium phosphate on TiO_2, Langmuir 15 (1999) 7355–7360.
[46] Y. Barbaux, M. Dekiouk, D.L. Maguer, L. Gengembre, D. Huchette, J. Grimblot, Bulk and surface analysis of a Fe–P–O oxydehydrogenation catalyst, Appl. Catal. A: Gen. 90 (1992) 51–60.